Experiments in Fluids 24 (1998) 447–461 © Springer-Verlag 1998

Investigation of aerodynamic effects of coolant ejection at the trailing edge of a turbine blade model by PIV and pressure measurements

M. Raffel, F. Kost

Abstract In order to simulate the thick trailing edges of turbine blades a slotted plate profile together with a newly designed nozzle was installed into the high-speed wind tunnel of the DLR Göttingen. At different supersonic Mach numbers and at four coolant flow rates in the range of 0–2.5% pressure distribution measurements and probe measurements were performed. The flow field was visualized by schlieren photos and the instantaneous velocity field was quantitatively investigated by Particle Image Velocimetry (PIV). The measurements of the velocity field gave an insight into stationary effects, for example the change of shock strength with coolant flow rate, and instationary effects such as the existence of a vortex street in the wake. The PIV technique offers special advantages for the investigation of transonic flow fields, but also yields to special experimental difficulties, which are also described in this article. Measured losses display a maximum at the downstream Mach number 1. This is strongly related to the behaviour of the base pressure. A loss minimum is achieved at moderate coolant flow rates, showing that an optimum coolant flow rate exists. The loss was analysed and separated into the loss contributions from the profile upstream of the trailing edge and the mixing loss due to the coolant flow.

1 Introduction

The flow at the thick trailing edge of a turbine blade produces high losses, especially in the transonic flow regime (Sieverding et al. 1980; Sieverding 1982; Kost and Holmes 1985; Denton and Xu 1989; Mee 1992). In the frame of the joint German research program "AG-TURBOTECH" a special task dealt with the aerodynamic effects of coolant ejection at a model trailing edge.

The schlieren photo, Fig. 1, gives an insight into the typical transonic/supersonic flow field at the rear part of a gas turbine profile. The base region containing recirculating fluid ends in a recompression zone where two shocks are generated. One of these shocks hits the suction side of the neighbouring blade and interferes with the suction side boundary layer. The boundary layers at the trailing edge coming from the suction or from the pressure side are therefore different and a model experiment to simulate a turbine trailing edge has to take that into account. The low energy fluid in the base region is extremely sensitive to spanwise pressure gradients. Therefore a wind tunnel enabling a large span of the model blade is needed in order to establish two-dimensional flow.

The goals of the flow field measurements were: quantitative determination of the structure of the wake and of the trailing edge shock system at various coolant flow rates. Additionally, the experimental results were supposed to yield comprehensive information for optimization and validation of numerical codes for two-dimensional numerical simulations, which shall serve as a tool for blade design in future. Therefore, the measurements described here were performed by means of particle image velocimetry (PIV). This technique was found to be well suited, as the investigations had to be carried out for several Mach numbers and coolant flow rates of the cooling air within very short time intervals. The instantaneous recording of the flow velocity fields does not only save tunnel operating time and costs, but also enables the study of non-stationary effects. However, the PIV technique does not only offer special advantages, but also yields to special experimental difficulties, which will be described in Chap. 3. Wind tunnels usually used for the study of plane turbine cascades allow only small models (e.g. EGG of DLR in Göttingen: chord $c_1 = 60$ mm, spanwidth $s = 125$ mm). Since thick trailing edges were needed for adequate instrumentation with pressure probes, our experiments have been conducted in a larger facility. The configuration used was similar to one used at VKI in Brussels (Sieverding et al. 1976; Sieverding et al. 1980; Sieverding 1982) but much larger. Systematic measurements in straight cascades of the afore mentioned authors have shown a strong correlation between the pressure at the base of the trailing edge and the downstream pressure. They have demonstrated that such a simulation of the trailing edge flow without cooling air ejection yields realistic results. Schlieren images and pressure measurements of a symmetric flow field at an enlarged trailing edge model with cooling air ejection have been performed

Received: *12 May 1997*/*Accepted*: *13 October 1997*

M. Raffel, F. Kost
Institut für Strömungsmechanik
Deutsche Forschungsanstalt für Luft- und Raumfahrt (DLR)
Bunsenstraße 10, D-37073 Göttingen, Germany

Correspondence to: M. Raffel

The authors would like to thank the team of WT-WK-HKG Göttingen for their help during the wind tunnel tests. The work of our PIV team especially of Mr. Höfer is greatly appreciated. This research project was supported by the German Ministry of Education, Science, Research, and Technology (BMBF) by the grant 'No: 0326800F'. The authors are responsible for the content of this publication.

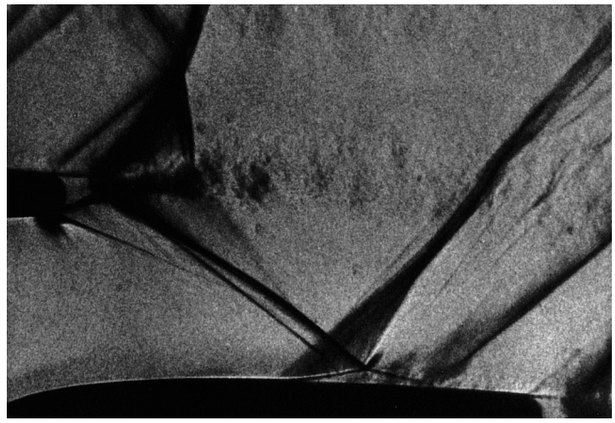

Fig. 1. Typical transonic/supersonic flow field at the rear part of a gas turbine profile

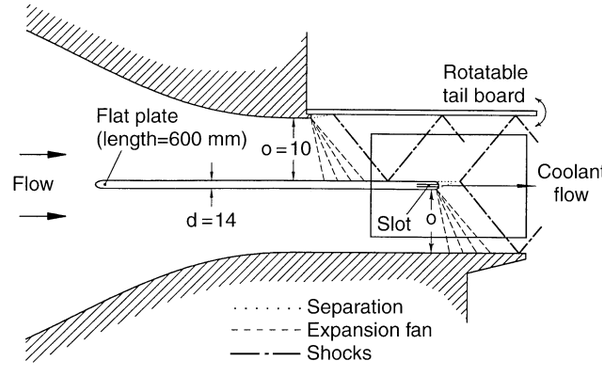

Fig. 2. Flat plate model installed in the wind tunnel and sketch of a supersonic flow case

by Motallebi and Norbury (1981), in order to investigate the relationship between the vortex formation and the base pressure. Their schlieren images yielded important information about the flow phenomena at the trailing edge. It has been shown, that a Karman vortex street can only be observed at low coolant flow rates. Molezzi and Dutton (1993) have successfully applied the PIV technique in the separated wake region behind a two-dimensional base model in a Mach 0.4 flow, revealing features of the von Kármán vortex street wake and underlying small-scale structures in great detail.

2
Experimental facility

The turbine blade trailing edge model was set up in the high-speed blow-down wind tunnel (HKG) of DLR in Göttingen. Here, transonic flow velocities can be obtained by sucking air from an atmospheric intake into a vacuum tank. A quick-acting valve, located downstream of the test section, is quickly opened to start the flow. Ambient air, which is dried before entering the test chamber, flows for max. 20 s through a test section with 725 mm spanwise extension. Grids in the settling chamber and a high contraction ratio of more than 20:1 lead to a low turbulence level in the test section.

Figure 2 shows the trailing edge model in the wind tunnel. Due to specially adapted wind tunnel walls above and below the model, and an adjustable tailboard above the model, the flow field with structures as described in the following could be obtained. On the lower side of the model the flow accelerates continuously down to the trailing edge. On the upper side the Mach number distribution has positive and negative gradients. Downstream of the smallest cross section Mach number values between $Ma = 0.9$ and 1.8 can be observed depending on the prior defined angle of the tailboard. The expected flow phenomena are also shown in Fig. 2.

The step between the contour of the upper wall of the nozzle and the tailboard simulates the trailing edge of the neighbouring cascade blade. The step generates a separation bubble, an expansion fan, and the subsequent oblique compression shock. The tailboard can be adjusted to a predefined angle, which defines the downstream flow direction and therefore also the outlet Mach number downstream of the model trailing edge. The tailboard angle also determines the maximum Mach number and the strength of the shock impinging on the upper surface of the model. The line from the above mentioned step to the trailing edge of the model plate is quasi the blade gap of the fictitious turbine cascade we intend to simulate. The upper side of the blade therefore simulates the suction side of the turbine blade downstream of the smallest cross-section, whereas the lower side represents the pressure side. The planar section of the lower nozzle contour is to simulate the suction side of the next blade of the cascade.

A slot in the trailing edge with a width of 4 mm serves to eject air into the base region simulating coolant ejection. The nozzle, the plate and especially the trailing edge are equipped with a great number of pressure tappings which are all located near mid span. Downstream of the plate, at the x-position of the end of the glass windows but in mid span, a probe rake could be installed, mainly equipped with pitot probes but also including two wedge probes. A total number of 110 pressure measurements could be recorded simultaneously using a PSI pressure measurement system.

3
PIV technique

In the past years the PIV method has gained continual acceptance as a valuable fluid mechanics research tool in a wide variety of applications. A summary of the theoretical and experimental aspects of the PIV technique is given by Adrian (1991). In this section the PIV subsystems specially developed for application in transonic flows will be described. First of all *tracer particles*, generated by an aerosol generator, have to be added to the flow. These particles have to be *illuminated* in a plane of the flow twice within a short time interval. The light scattered by the particles has to be *recorded*. The displacement of the particle images between the two light pulses has to be determined at the *evaluation* of the PIV recordings. In order to be able to handle the great amount of data, which are collected by employing the PIV technique, a sophisticated *post processing* system is required.

3.1 Tracer particles

First applications of PIV have already shown that difficulties appear providing high quality seeding in high speed air flows compared to applications in water flows or in low speed air flows (Höcker and Kompenhans 1991; Towers et al. 1991; Humphreys et al. 1993; Molezzi and Dutton 1993). High speed air flows require small tracer particles in order to minimize the velocity lag. This problem is discussed in literature intensively (Hunter and Nichols 1985; Melling 1986; Meyers 1991). However, by decreasing the particle size the light scattered by the particles will be reduced considerably. Thus, a modern high power pulse laser is necessary for recording of tracer particles with a diameter of one micron or less. A much larger volume has to be seeded for PIV than for LDA as the flow velocity is not only measured at a single point but in a whole plane. Moreover, for PIV there should be no gaps in the seeding, as this would lead to data dropout in the instantaneous velocity field. It is known from simulations of the PIV evaluation process, that typically 15 particles per interrogation volume are essential for a high quality evaluation (Keane and Adrian 1990). In order to keep constant the number of particles per PIV recording, more particles have to be added to the flow with increasing flow velocity. Thus, a powerful aerosol generator is required for transonic flows. For our experiments we have utilized several Laskin nozzles in parallel. This proved to be sufficient to seed a large stream tube surrounding the model and the observation area. Finally we could attain a high density of tracer particles of the order of up to 4 particles/mm^3 (this corresponds to ≈ 30 particles per interrogation volume) during the experiments. The aerodynamic diameter of the olive oil particles was about 1 μm (Schäfer 1995). It is well known from LDA measurements in large wind tunnels and in high speed flows, that the size and the distribution of the tracer particles may change during the travel from the aerosol generator to the seeding device in the settling chamber of the wind tunnel and, finally, to the test section, where the measurements take place. It is therefore advisable, to gain information about the particles and especially about the velocity lag directly from the observation area. This has been done during prior tests in a transonic flow field around a bluff cylinder in the same wind tunnel (Kompenhans and Raffel 1993). This test showed that it does not make much sense to utilize tracer particles with a diameter much smaller than 1 μm for such experiments, because the spatial resolution of the velocity measurement is not limited by the response of a particle to a velocity gradient, but due to the fact that during the evaluation of a PIV recording the velocities are averaged within each interrogation spot (width of a shock $\approx$ a few micrometers, width of an interrogation volume $\approx$ a few millimeters). Smaller tracer particles would be necessary only, if e.g. a higher spatial resolution in the vicinity of the shock would be required.

In contrast to prior high speed PIV applications, the measurements described here were additionally complicated by the fact that the air ejected from the trailing edge had also to be seeded. Therefore, tracer particles had to be generated against a pressure level of 4 bar. The seeded air passed a distributor system that contained tiny nozzles inside the model where supersonic flow conditions were obtained. Therefore, some particles have been precipitated inside the model and have left the outlet from time to time in form of larger droplets. Recordings on which those droplets have been observed have not been evaluated. Figure 3 shows a part of a PIV recording obtained at $Ma_2 = 1.27$ and a coolant flow rate of 1.4%. On the left hand side parts of the contour of the trailing edge model can be seen twice due to image shifting applied between exposures. The recording further illustrates some of the above mentioned problems: Varying intensity of the particle images due to droplet formation inside the ejected air stream and a reduced seeding density directly above and below the model due to the influence of the boundary layers along the plate.

Fig. 3. A part of a PIV recording at $Ma_2 = 1.27$ with the model contour on the left hand side

3.2 Illumination system

A double oscillator Nd:YAG pulse laser was used for illumination. The output energy was approximately 2×40 mJ during these measurements. This energy was sufficient to illuminate a sheet with a height of 20 cm, when recording the light scattered by the 1 μm particles on a highly sensitive photographic film. The time delay Δt between the two laser pulses was set to 4 μs for these experiments. The optical access to the test section was complicated by the fact that the test chamber of the wind tunnel is generally on a pressure level below the atmospheric pressure during the tunnel run. Therefore, the laser was located outside the tunnel, whereas the light sheet optic was mounted onto the floor of the test chamber. The light was directed into the tunnel through a small orifice in the wall. The optical path between laser and observation area had a length of more than 5 m. The last mirror was located 1.5 m downstream of the model and close to the shear flow of the open test section. The size of the observation area was approximately 100×150 mm^2. The light sheet thickness was adjusted to ~ 0.5 mm. The sheet was oriented normal to span direction in mid span.

3.3 Recording

Today, an almost immediate availability of the PIV data is possible by using video based approaches for PIV recording.

However, this advantage is opposed by a reduction in spatial resolution such that the photographic recording method continues to be a valuable tool for high resolution PIV measurements. Therefore, we used the photographic technique which required some special developments not commercially available. One major problem is associated with the limited amount of light scattered by the small tracer particles. Typically, the depth of focus at recording is of the order of 1 mm in our experiments, which means that the intensity of the light as scattered by out-of-focus particles is not high enough to expose the photographic material sufficiently.

Focusing

Already PIV experiments in large wind tunnels have shown that a high quality and reliable focusing device is necessary, in order to save time during the alignment of the system. For this purpose our photographic 35 mm camera is equipped with a device for fast focusing (Kompenhans and Raffel 1993). A CCD sensor with high spatial resolution was mounted in the viewfinder of a SLR camera, yielding an image of a small part in the center of the observation area. The position of the CCD sensor is carefully aligned in such a way that the distance between lens and sensor via the mirror is exactly the same as from the lens to the film plane. The distance between light sheet and film plane can be changed by moving the complete camera system by means of a traversing table, while observing the diameter of the particle images on a TV monitor.

Imaging of small particles in transonic flows

This section describes the limits of imaging due to diffraction and lens abberations, which is a problem of particular interest for PIV recording in aerodynamics. The theoretical minimum diameter of an image which can be obtained is:

$$d_i = 2.44\, f_{\#}\,(M+1)\,\lambda$$

where M is the magnification (image distance/object distance), $f_{\#}$ the focal length f divided by the aperture diameter D_a, and λ the wave length of the laser light (for details see Goodman 1968).

In PIV, the minimum image diameter d_i will be obtained only, when recording small particles at small magnifications. For larger particle image diameters d_p and/or larger magnifications the influence of geometric imaging becomes more and more important. The image of a finite-diameter particle is given by the convolution integral of the point spread function with the geometric image of the particle. Approximating both functions leads to the following formula for the image diameter (Adrian and Yao 1985):

$$d_{pi} = \sqrt{d_g^2 + d_i^2}$$

wherein $d_g = M d_p$ if the lens is well focused. The following formula can be used to estimate the enlargement of the geometric image diameter Δd_g of an image point as a function of the difference ΔB between object distance employed and object distance needed for sharp imaging.

$$\Delta d_g = \frac{M^2 \Delta \mathrm{B}}{\mathrm{f}_{\#}\,(M+1)} \quad \text{(after Solf 1975)}$$

Table 1. Values for diffraction limited imaging ($\lambda = 532$ nm, $M = 1/4$, $d_p = 1$ µm)

$f_{\#} = f/D_a$	d_{pi}[µm]	δ_z[mm]
2.8	4.7	0.5
4.0	6.6	1.1
5.6	9.1	2.0

The following formula can be used to estimate the depth of field, if assuming that an enlargement of the geometric image diameter Δd_g smaller than the minimum diameter due to diffraction limited imaging d_i can be tolerated:

$$\delta_z = 2 f_{\#}\, d_i (M+1)/M^2$$

Some typical values for the diffraction limited imaging of small particles ($d_p \approx 1$ µm) are shown in Table 1 (calculated with a wavelength of $\lambda = 532$ nm, a magnification of $M = \frac{1}{4}$). It can be seen in Table 1, that a large aperture diameter is needed to get enough light from each individual particle within the light sheet, *and* to get sharp particle images, because the size of the diffraction pattern can be decreased by increasing the aperture diameter. Unfortunately a big aperture diameter yields a small focal depth which is a significant problem when imaging small tracer particles.

In practice there are two good reasons for minimizing the particle image diameter: *First*, a detailed analysis of PIV evaluation shows, that the error in velocity measurement can be reduced by minimizing both the image diameter d_{pi} and the uncertainty in locating its centroid (Adrian 1986a).

Second, sharp and small particle images are particularly essential in order to obtain a high particle image intensity I, since the light energy per unit area increases with decreasing image areas ($I - 1/d_{pi}^2$). If the light energy contained in a single particle image is spread over a large area, it might not expose the sensor or film sufficiently.

Since lens abberations also have a great influence on the recording of small objects, high quality lenses are essential for PIV. A useful tool in evaluating the performance of a lens is the modulation transfer function (MTF). The MTF has become a widely used means of specifying the performance of lens systems and films (Hecht and Zajac 1974) and can be used to analyse the influence of lens abberations on the PIV recording. Values of the modulation transfer are often given in the data sheets of a lens system for different f-numbers and magnifications or can easily be estimated when studying diagrams of the modulation versus the image height. From our experience these values can be used for a rough estimation of the image diameters to be expected, regardless of the fact that they were originally measured using white light and therefore also consider chromatic aberrations.

The modulation transfer value of high spatial frequencies r' can be taken to determine the minimum image diameter d_i by using the following formula:

$$d_i \approx \sqrt{0.64 \frac{-\ln(\tilde{M}_{TF}(r'))}{r'^2} - \left(\frac{M}{2r'}\right)^2} \quad \text{(Raffel et al. 1996).}$$

The definition of a MTF is a practical approach to describe optical processes, which in reality are much more complex. However, for many practical applications the overall MTF of an optical system can be assumed to be simply the product of the MTF's of the individual components. Therefore, the value of the film MTF can be multiplied with lens MTF value for the same spatial frequency r' and the above equation can be used to estimate the image diameter for a given recording condition. Practical experience has shown that the resolution of a film with high sensitivity (3200 ASA) and a modulation transfer of $\approx 80\%$ at 40 line pairs/mm can be used to perform high quality PIV measurements even in the case of difficult recording conditions (Kompenhans and Raffel 1993). The image diameter estimated by the above equation is ≈ 20 μm ($M=\frac{1}{4}$, $f_{\#}=2.8$) and is in good correspondence with image diameters found during the experiments.

However, inspecting the PIV recordings of this experiment under the microscope has shown that sharp particle images can not be found in the vicinity of the oblique shocks and close to the trailing edge. In a very small area where the oblique shocks are imaged no particle images could be observed at all. This area did not lead to a significant data drop out, however, since its width was small with respect to the width of the interrogation window. More severe problems occur in the area directly behind the trailing edge. Only a few large particle images were found here (see Fig. 3). From schlieren images (see Fig. 1) and pressure measurements it is known that very high density gradients appear there.

In order to estimate the influence of the density variations in the flow field onto imaging we determine the variation of the refractive index Δn using the Gladstone–Dale equation:

$$n-1=G(\lambda)\rho$$

wherein $G(\lambda)$ represents the Gladstone–Dale-number and ρ the density of the fluid. $G(\lambda)$ for our laser light ($\lambda=532$ nm) has been estimated by formula

$$G(\lambda)=2.2244\times10^{-4}\frac{m^3}{kg}\left(1+\left(\frac{6.7132\times10^{-8}\,m}{\lambda}\right)^2\right)$$

(Oertel and Oertel 1989)

The following estimation of the density effects is based on assumptions which are not valid in general, but allow us to model the imaging of the base region, which was located close to the center of the observation area and therefore in the vicinity of the optical axis of the lens. We assume a particle located in the object plane at position X and a density step due to a compression shock at position X_S (see Fig. 4). For X_s larger than half the aperture diameter the rays through the upper and the lower edge of the aperture will be deflected in the same direction. This can result in a slight displacement of particle images, but this effect is expected to reduce the sharpness of the images in only a minor way. For X_s smaller than half the aperture diameter we can estimate the enlargement of the geometric particle image diameter by tracing two rays which are forming the image and determining their displacement in the image plane: $\Delta d_g=x_2-x_1$. When tracing the ray of scattered light propagating parallel to the optical axis, density variations can be neglected and standard imaging condition are valid resulting in $x_1=MX$ where M is the magnification

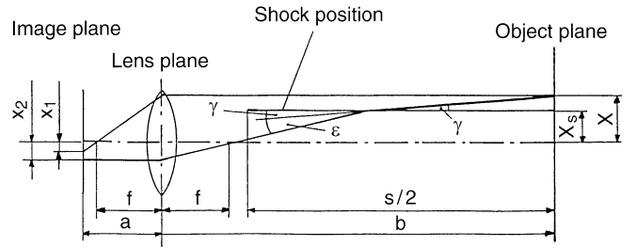

Fig. 4. Diagram of imaging (shock wave and particle position close to the optical axis)

factor. The ray incident on a compression shock – considered as a plane interface of two media of refractive indices n_1 and n_2 – under a small angle γ will be deflected towards the medium with higher density under an angle of $(\gamma+\varepsilon)$ with respect to the interface (Fig. 4). For small variations of the diffraction index the following equation can be obtained as a solution of Snell's law of refraction:

$$\varepsilon=\sqrt{2(\Delta n/n_1)+\gamma^2}-\gamma$$

This equation shows that ε increases with decreasing γ and for $\lim_{\gamma\to0}\varepsilon$ converges to $\sqrt{2(\Delta n/n_1)}$. From Fig. 4 it can be seen that $x_2=f\tan(\gamma+\varepsilon)$. The displacement of two rays in the image plane in worst case ($X=X_S=(b-f-s/2)\tan(\varepsilon)$). Therefore, the enlargement of the geometric particle image can be approximated by:

$$\Delta d_g=(f-M(b-f-s/2))\tan(\sqrt{2(\Delta n/n_1)}).$$

Using the aforementioned equations and assuming $P_1/P_2\approx0.5$ which corresponds to values found during the experiments yields: $n_2=2\times10^{-4}$ and $n_1=1\times10^{-4}$. Using $M=0.2$, $f=$ 100 mm, $s/2=362.5$ mm and the lens equations $1/f=1/a+1/b$ and $M=a/b$ results in:

$$\Delta d_g=1025\ \mu\text{m}$$

It has to be mentioned that the determination of Δd_g based on the assumption of a step in the refractive index of the flow medium might be too pessimistic. Although the extent of strong compression shocks is much smaller than the scale of other flow structures, it can be a few times larger than the wavelength of the laser light. This fact could be taken into account by a quantitative estimation of diffraction effects, enabling the density gradients due to vortex formation in the base region to be considered. However, our aim was to show that the variation of refractive index in transonic flow fields can result in unsharp imaging if the optical path is parallel to shock waves (e.g. in the center of the observation area). This fact limits the quality of PIV recording in 2d-flow facilities because there the observation angle can not be changed easily due the size and location of the schlieren windows which give the optical access to the flow. However, the situation might be improved using oblique observation angles and Scheimpflug recording configurations to ensure focusing.

Image shifting

Another problem becomes obvious from the description of the recording process as given above, i.e. the direction of the motion of the particles within each interrogation spot can not be determined if employing the 'dual illumination-single frame' recording technique since there is no way to decide which image is due to the first and which is due to the second exposure of a particle. Although, for many applications the sign of the velocity vector can be derived from a priori knowledge of the flow, in reverse flows, for example in areas of detached flow and in wakes behind models, steps have to be taken to determine the sign of the displacement and hence the velocity vector correctly. The great interest in PIV measurements in many different fields of research requires a flexible technique for ambiguity removal which can be applied to a variety of experimental situations. For aerodynamic investigations it is especially important to be able to apply this technique at high flow speeds, i.e. with short time intervals of a few microseconds between both illuminations. The most straightforward approach is the recording of both exposures separately, e.g. on two video frames as described by Cho (1989) and their subsequent analysis by means of cross-correlation (Willert and Gharib 1991). However, in order to apply this 'single illumination-dual frame' recording technique high-speed video cameras are needed, which do not yet offer the spatial resolution needed for larger observation areas (Rouland et al. 1994; Raffel et al. 1995). A different method for ambiguity removal has to be used for photographic PIV. Such a method is the image shifting technique as described by Adrian (1986b), which enforces a constant additional displacement, which must be greater than the maximum displacement due to the reverse flow, on the images of all tracer particles at the time of their second illumination. At present the most widely used experimental technique for image shifting is to utilize a rotating mirror systems. The observation area in the flow is imaged onto the recording area in the camera via the mirror. The magnitude of the additional displacement of the images of the tracer particles depends on the angular velocity of the mirror, the distance between light sheet plane and mirror, the magnification of the imaging system and the time delay between the two illuminations, see Landreth et al. (1988). At the DLR a high speed rotating mirror system has been developed in order to be able to carry out measurements also in transonic flows. The frequency of rotation ranges from 1 to 100 Hz, thus covering a range of shift velocities from 5 to 500 m/s. A detailed analysis of the errors involved with image shifting by means of a rotating mirror has also been given by Raffel and Kompenhans (1995). The rotational speed of the mirror was set to 2400 rev/min during the experiments, resulting in a virtual shift velocity of 279 m/s.

3.4 Evaluation and post processing

Each PIV recording (24×36 mm^2 format) was interrogated in small sub areas (92×56 interrogation areas with a step size yielding an overlap of 50% along the x- and y-axis). The local displacement vector for the images of the tracer particles has been determined for each interrogation area by means of statistical methods. The projection of the vector of the flow velocity into the plane of the light sheet (2d velocity vector) was computed taking into account the time delay between the two illuminations and the magnification at imaging. Due to difficult recording conditions further improvements of the evaluation algorithms were required. Unlike the autocorrelation methods used in conventional evaluation systems, our improved digital evaluation system uses a cross-correlation between image interrogation areas, which are displaced with respect to each other. This method, first described by Keane and Adrian (1992), has been implemented into a fully digital evaluation system of photographic PIV recordings (Willert 1996). The digital approach significantly reduces processing time because there no longer is a need to produce a high-contrast contact copy of the recording prior to interrogation. As films can be developed and dried within an hour, there now are multiple chances for feedback into the experiment during the course of a day. After evaluation, a certain number of obviously incorrectly determined velocity vectors can usually be found by visual inspection of the raw data. In order to reject these incorrect data the raw flow field data have to be validated. For this purpose automatic algorithms have been developed (Raffel et al. 1993). They are based on a comparison of each vector with the mean of its eight nearest neighbours. The locally varying threshold for rejection is determined by the variance of the neighbouring vectors. These algorithms ensure with high level of confidence that no questionable data are stored in the PIV data set. If it can not be decided by application of the validation algorithm whether data are valid or not, questionable data were rejected.

The magnitude of the local flow velocities $|U(x,y)|$ finally obtained has been used to determine Mach number distributions $Ma\,(x,y)$ by the following equation:

$$Ma\,(x,y) = \frac{|U(x,y)|}{\sqrt{\kappa R T_0 - (\kappa-1)/2\,(U(x,y))^2}}$$

wherein R is the ideal gas constant, T_0 is the total flow temperature, and κ is the ratio of heat capacities C_p/C_v.

Vector operators have been applied to analyse the two-dimensional vector data as obtained by the evaluation process in more detail. As has been demonstrated by Höcker and Kompenhans (1991), the location of oblique and normal compression shocks can therefore be found by analysing the maximum values of the divergence distributions of PIV recordings. Depending on flow parameters and trailing edge geometry the wake flow of transonic turbine cascade blades appears to consist of vortex streets. Shedding frequencies and corresponding Strouhal-numbers have been investigated for different blade geometries by Heinemann et al. (1975) by means of an electro-optical device. As described in the following, the Strouhal-numbers can also be extracted by analysing the vorticity distribution computed from the PIV data. The vorticity operator was used for localization of the distinct vortices and their average displacement Δx_{vort}. The flow velocity at the centers of the vortices has been used to estimate their convection speed U_{conv}. The Strouhal-number is defined as:

$$Str = \frac{f_{\mathrm{shed}}\, d}{U_2}$$

wherein f_{shed} is the frequency of vortex shedding, d is the trailing edge thickness of the blade, and U_2 the downstream velocity. The shedding frequency has been estimated by:

$$f_{shed} = \frac{U_{conv}}{\Delta x_{vort}}$$

One statement should be made concerning the accuracy of the PIV technique. The absolute over-all accuracy of the PIV system depends on many different parameters and has to be checked separately for each experiment. There is no simple means available to check the accuracy of PIV measurements in transonic flows against another measuring technique. Thus, usually it is tried to determine the accuracy of each individual component of the PIV system to derive a statement about the over-all accuracy. It has to be distinguished between three different error sources: the first one influences all velocity vectors of a PIV recording in the same manner (e.g. the magnification factor at imaging, scale factor of the evaluation system), the second one influences each velocity vector in a different, but steady way (e.g. velocity lag of tracer particles, optical distortion of the lens system, out-of-plane velocity component, errors due to image shifting) – however, neighbouring vectors are affected in a similar way (Sinha 1988; Raffel and Kompenhans 1994), and the third would be random errors associated with e.g. the evaluation process (see e.g. Keane and Adrian 1990; Willert 1996). The first two error sources would affect the evaluation of spatial structures in the flow field only in a minor way. The random errors associated with e.g. the evaluation process can be reduced to a minimum when having imaged the particles sharply and using advanced evaluation systems. We can demonstrate the relative accuracy of our system by successfully resolving very weak spatial structures in flow fields with turbulence levels below 0.5%. In the case of the experiments described here, we estimate the noise error to be in the order of 1% of the mean flow velocity. An average of e.g. 100 PIV data sets for each condition could be computed in order to reduce this error. However, this would suppress also the information on the instationary effects of the flow as for example the vortex street. The most valuable information which can been obtained from the PIV data are the instationary fluctuations, which are strong enough that they can be distinguished from noise.

4
Pressure distribution measurements

In Fig. 5 some surface Mach number distributions from the rear part of the plate are presented. These are Mach number distributions at different downstream Mach numbers but without coolant ejection. The isentropic contour Mach number is derived from the measured surface pressures according to the following formula:

$$Ma = \sqrt{\frac{2}{\kappa - 1}\left[\left(\frac{P}{P_{01}}\right)^{(1-\kappa)/\kappa} - 1\right]}$$

wherein P_{01} is the total pressure, P is the local static pressure, and κ is the ratio of heat capacities C_p/C_v.

On the lower side of the plate (model pressure side) the Mach number remains more or less constant up to the trailing edge. On the upper side of the plate (model suction side) the flow is accelerated rapidly till a pressure minimum is reached. Then a strong decrease of Mach number takes place caused by the impinging shock (see Fig. 2), and finally a strong expansion of the flow around the trailing edge is observed both on suction and on pressure side.

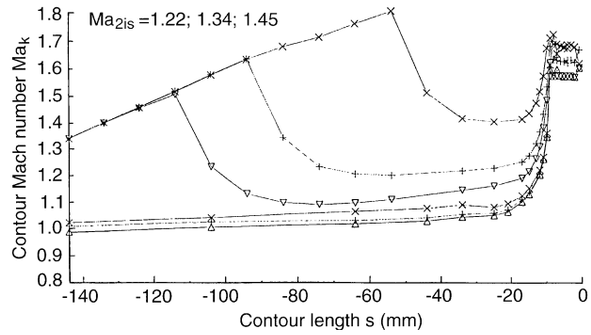

Fig. 5. Mach number distribution at model surface at different downstream Mach numbers

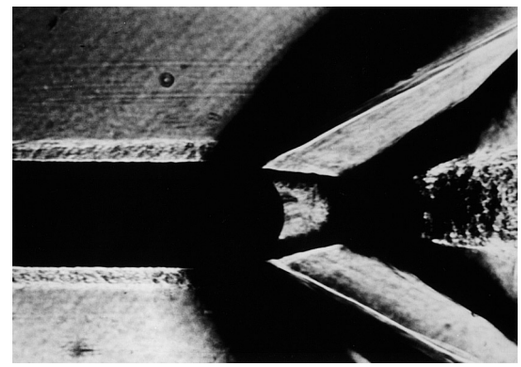

Fig. 6. Schlieren image at the trailing edge at $Ma_{2is} = 1.34$

The schlieren photo in Fig. 6 (schlieren edge vertical) gives a survey of the important flow phenomena near the trailing edge. A flash of roughly 30 ns duration was used yielding recordings of instationary events, too. First the turbulent boundary layers on suction and pressure side can be clearly seen. Already before the round trailing edge begins, the flow is accelerated which causes the black expansion fans seen in the photo. The expansion fans end abruptly at the points on the contour where the flow separates. Also at the beginning of the separation a weak oblique shock may be observed (light line at the end of the expansion fan). Dark separation lines mark the boundaries of the base region containing recirculating fluid. At the end of the recirculating fluid region where the fluid streams from both sides of the profile interfere, oblique shocks are generated. Downstream of these recompression shocks there is locally subsonic flow which makes the generation of von Karman vortices possible. In any case much turbulence energy is produced by the mixing of the shear layers downstream of the trailing edge, and this is why a highly turbulent wake is visible.

The following figure gives a detailed picture of the development of static contour pressures around the trailing edge.

Figure 7 displays surface pressures at different downstream Mach numbers but without coolant ejection. Beginning from the high pressure level on the suction side the flow expands rapidly around the trailing edge. The expansion starts well in front of the circular trailing edge – clearly a viscous effect, as in inviscid supersonic flow the expansion would start just at the beginning of the half circle. A pressure minimum is reached at the point of flow separation where a zone of constant pressure follows – the so called base pressure p_b. A small pressure jump between pressure minimum and base pressure is observed which is caused by a weak oblique shock at the separation point as mentioned in the previous paragraph. On the pressure side a nearly universal expansion curve exists i.e. the measured points for all four downstream Mach numbers lie on one curve. This behaviour consequently leads to separation locations which lie further downstream the lower the base pressure is (see Table 2).

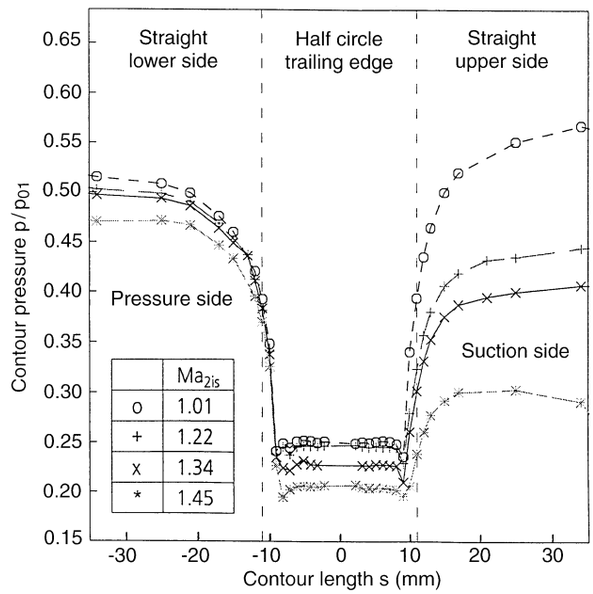

Fig. 7. Static pressure distributions at the model trailing edge without coolant ejection

The development of the surface pressures on the suction side is qualitatively similar to the pressure side. The main difference is that the expansion starts from rather different pressure levels. There is one peculiar fact however: the separation location is the same for all the four investigated downstream Mach numbers (see Table 2), though the expansion curves have different gradients and end at different base pressures. The following table lists some characteristic values of coolant and base flow. Base pressure coefficient is defined as follows:

$$c_b = \frac{P_b - P_2}{P_{02} - p_2}$$

The location of separation is listed as a contour length coordinate s and as an angle α. The values indexed with an a represent values at the outlet slot, S values on the suction and D on the pressure side. As shown in Fig. 7 the contour length coordinate s and α are defined negative on the pressure side and zero at the trailing edge. The contour length coordinate s is 11.0 and $\alpha = \pm 90^\circ$ at the point where the round trailing edge begins.

Static pressure distribution for different flow rates have been evaluated to analyse the effect of coolant ejection on the base pressure. The general effect of small coolant flow rates is to raise the base pressure. At higher coolant flow rates the base pressure is lowered again. Low momentum coolant flow is able to fill up the wake, but higher momentum coolant flow obviously acts like an ejector, it accelerates the base region fluid and so lowers base pressure. In Fig. 8 base pressures and base pressure coefficients are displayed.

Table 2. Characteristic values of coolant and base flow

Ma_{2is}	Coolant flow				Base pressure		Separation location			
	c_m %	$\frac{(\rho w)_a}{(\rho w)_2}$	Ma_a	$\frac{p_{0a}}{p_{01}}$	$\frac{p_b}{p_{01}}$	c_b	s_D [mm]	s_S [mm]	α_D [°]	α_S [°]
1.01	0	0	0	0.250	0.2495	−0.663	−9.1	9.1	−75	75
1.05	2.5	0.728	1.0	0.688	0.3072	−0.421	−8.5	9.1	−70	75
1.22	0	0	0	0.244	0.2440	−0.299	−9.1	9.1	−75	75
1.22	0.8	0.239	0.392	0.356	0.3200	−0.157	−9.1	10.0	−75	82
1.23	1.4	0.421	0.642	0.440	0.3335	−0.122	−9.1	10.0	−75	82
1.21	2.5	0.752	1.0	0.688	0.2727	−0.261	−9.1	9.1	−75	75
1.34	0	0	0	0.226	0.2255	−0.191	−8.1	9.1	−66	75
1.35	0.8	0.247	0.443	0.322	0.2814	−0.091	−9.1	9.9	−75	81
1.36	1.4	0.437	0.765	0.406	0.2755	−0.092	−9.1	10.0	−75	82
1.35	2.5	0.781	1.0	0.688	0.2205	−0.189	−8.1	9.1	−66	75
1.45	0	0	0	0.204	0.2044	−0.147	−8.1	9.1	−66	75
1.45	0.8	0.260	0.489	0.300	0.2544	−0.060	−9.1	10.0	−75	82
1.45	1.4	0.457	0.867	0.391	0.2396	−0.082	−9.1	10.0	−75	82
1.45	2.5	0.822	1.0	0.688	0.1807	−0.176	−8.1	9.1	−66	75

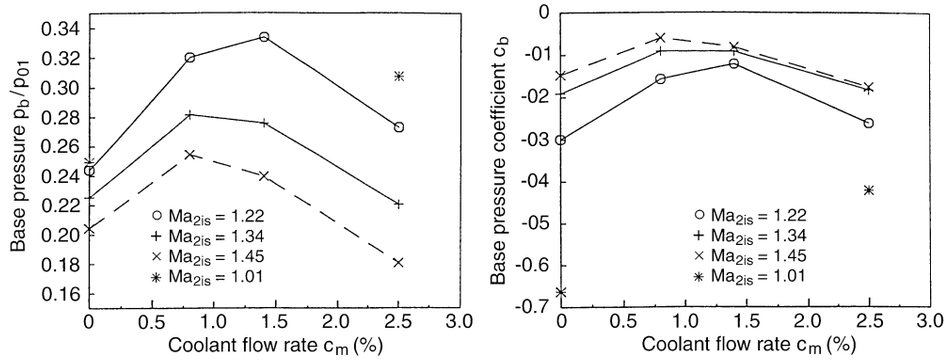

Fig. 8. Base pressure values and base pressure coefficients

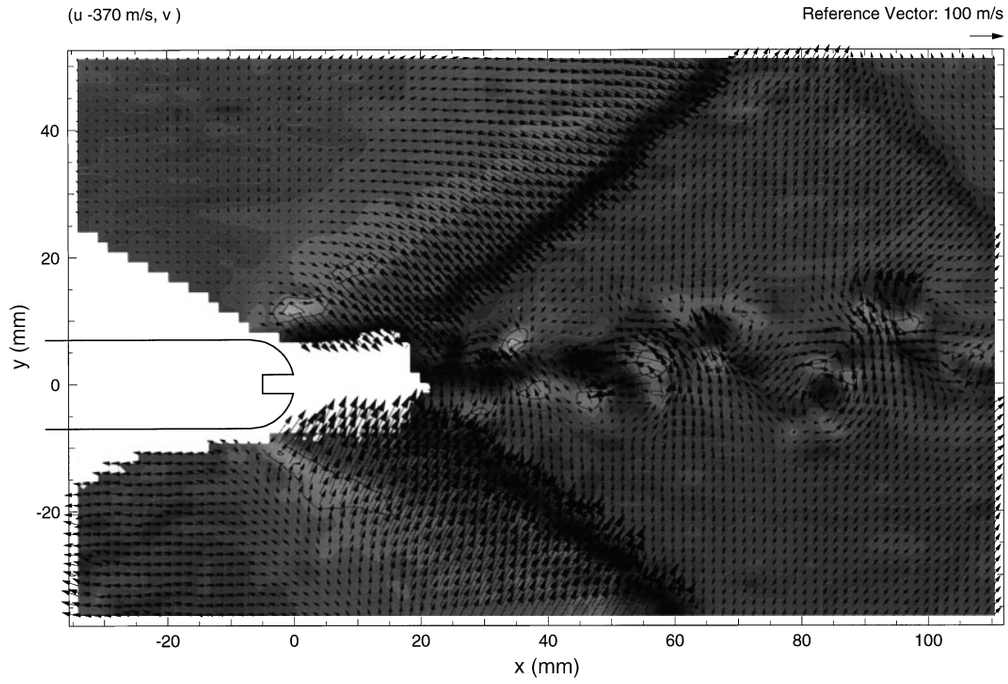

Fig. 9. Velocity vector plot and divergence distribution (grey values) derived from a PIV recording at a downstream Mach number $Ma_2 = 1.27$ and a coolant flow rate of 0%

5
Results from PIV measurements

Measurements of the flow field have been taken at two different cascade downstream Mach numbers ($Ma_2 = 1.17$ and $Ma_2 = 1.27$ resp. $Ma_{2is} = 1.22$ and $Ma_{2is} = 1.34$) and at four different coolant flow rates (0%, 0.8%, 1.4%, 2.5%). The coolant flow rate is defined as the ratio between the coolant flow of the cooling air and the coolant flow between two blades. The following results at $Ma_2 = 1.27$ will be shown and described briefly. The vector plots represent the measured velocity vectors. The influence of the mirror image shift has already been removed. An arbitrarily chosen velocity has been subtracted from the u-component of each individual velocity vector in order to enhance the velocity fluctuations for better representation.

Figure 9 shows the instantaneous flow velocity field at the trailing edge without coolant ejection. Expansion waves and terminating shocks can easily be seen. The distribution of velocity divergence in the observation area (grey value coded) allows an easy detection of the shock waves, due to the strong velocity gradients. The point of intersection of both main shock waves was located 10 mm behind the trailing edge of the model. A shock reflected from the tailboard above the observation field can be seen on the upper right hand side. The wake is characterized by a vortex street. A Strouhal-number of $Str \approx 0.38$ was determined by the procedure described above. This value indicates the unsteady behaviour of the wake flow, and agrees well with Strouhal-numbers measured by Heinemann et al. (1975).

The following changes in the velocity field can be observed for a cooling air coolant flow rate of 0.8% (see Fig. 10). The strength of the shock wave is significantly reduced. The negative velocity gradients, which follow the expansion waves below and above the trailing edge, cover relatively large areas.

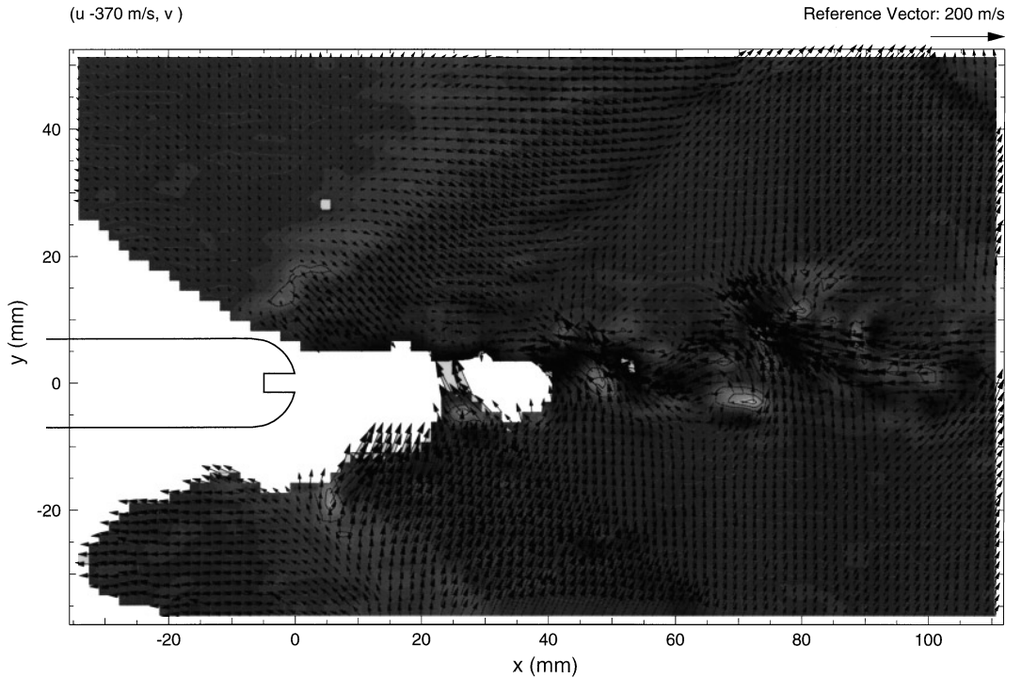

Fig. 10. Velocity vector plot and divergence distribution (grey values) derived from a PIV recording at a downstream Mach number $Ma_2 = 1.27$ and a coolant flow rate of 0.8%

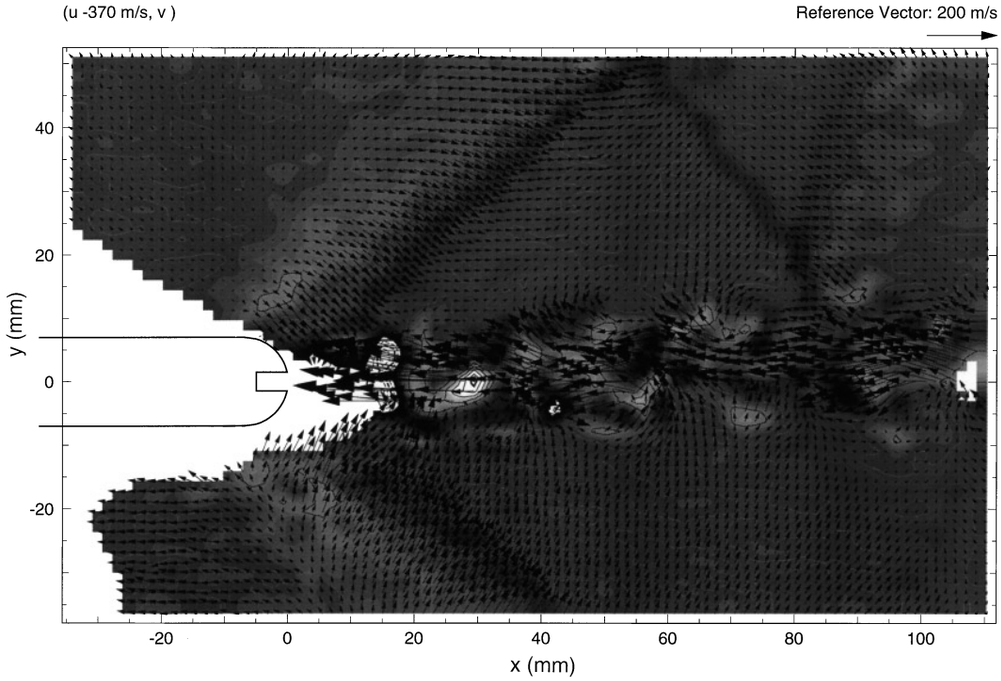

Fig. 11. Velocity vector plot and divergence distribution (grey values) derived from a PIV recording at a downstream Mach number $Ma_2 = 1.27$ and a coolant flow rate of 1.4%

On the upper side two expansion and compression waves can be observed. The wake flow is separated by two shear layers from the main flow in which some distinct vortices can be observed.

For a further increased coolant flow rate of 1.4% the shock intensity was again relatively strong. Furthermore, on the upper right hand side of the observation area two further shock waves can be detected (see Fig. 11). The oblique shock has been

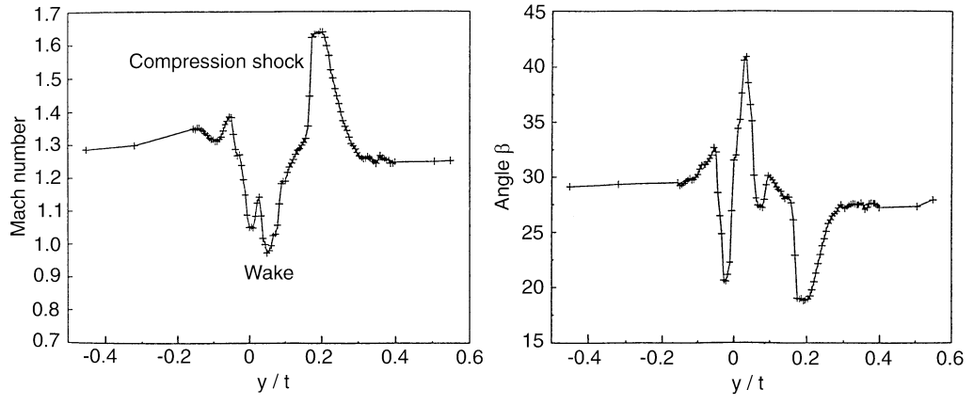

Fig. 12. Cut through the flow field parallel to the "cascade exit plane" at downstream Mach number $Ma_2 = 1.27$; coolant flow rate 0%

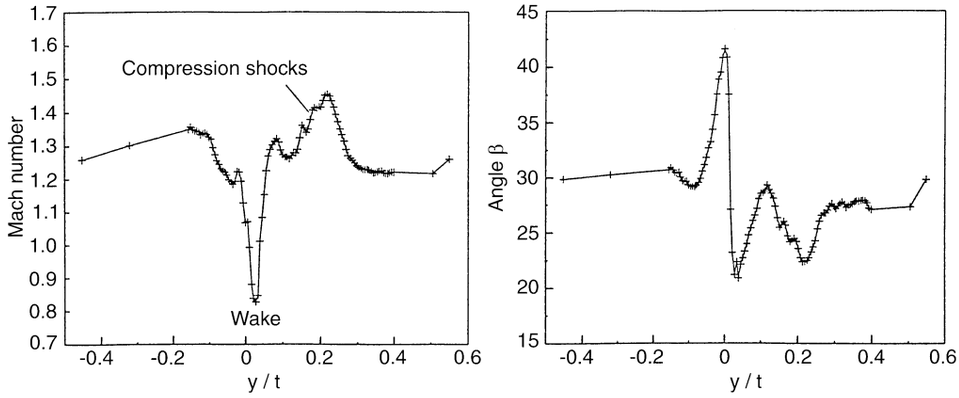

Fig. 13. Cut through the flow field parallel to the "cascade exit plane" at downstream Mach number $Ma_2 = 1.27$; coolant flow rate 0.8%

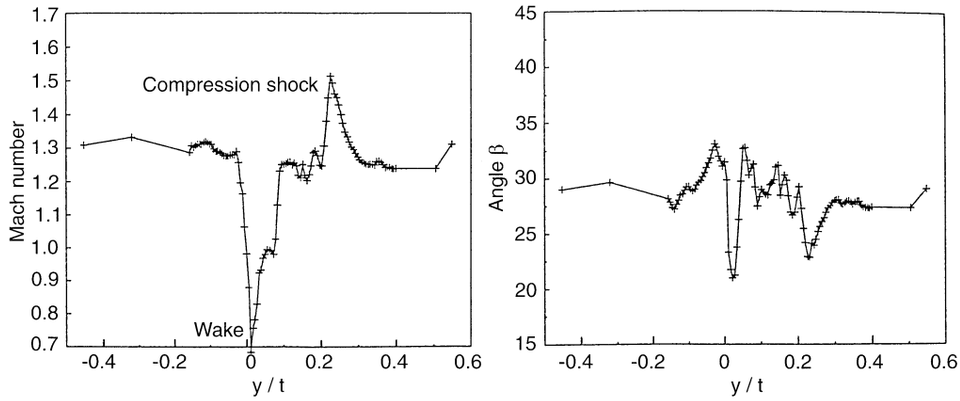

Fig. 14. Cut through the flow field parallel to the "cascade exit plane" at downstream Mach number $Ma_2 = 1.27$; coolant flow rate 2.5%

reflected at the tailboard above the observation field. This shock wave was again reflected at the wake of the model. This yields the vertical line of maximum divergence values at the right hand edge of the observation field. Varying positions of the shock reflected at the wake can be seen when comparing different PIV measurements taken at the same tunnel run and for the same parameters.

The line from the corner in the upper nozzle to the model trailing edge is a fictitious cascade exit plane (see Fig. 2). Figures 12, 13 and 14 show Mach numbers and flow angles, measured by PIV, on a line parallel to this "cascade exit plane". The y-coordinate goes upwards, so first the wake is cut and then one of the oblique shocks coming from the trailing edge (see Fig. 9). The flow in the wake is instationary and therefore strongly oscillating in the PIV snap shot. The shock seems to be quite stationary and with coolant flow absent (Fig. 12) the shock may be recognized as a distinct Mach number and angle discontinuity. At a coolant flow rate of 0.8% instead of one shock two weak oblique shocks are produced (Fig. 13), whereas at coolant flow rate 2.5% (Fig. 14) the shock seems to be strong again. Therefore it is clear that a loss minimum should occur at a moderate coolant flow rate.

6
Homogeneous flow values

With the aid of the velocities measured by PIV and pressures measured by probes, for every measurement a homogeneous downstream Mach number, downstream angle and loss may be computed. On a line parallel to the "cascade exit plane" the inhomogeneous flow values are mixed out by applying the equations of conservation of mass, momentum and energy (Amecke and Safarik 1995), giving the homogeneous flow static pressure p_2, the homogeneous total pressure p_{02} and the angle. After this data reduction the cascade parameters like isentropic Mach number Ma_{2is} and the cascade losses are known. As a loss parameter the energy loss derived from enthalpy h is used (see Horlock 1966)

$$\xi = 1 - \frac{h_{02} - h_2}{h_{01} - h_{2is}} = 1 - \frac{W_2^2}{W_{2is}^2} = 1 - \frac{1 - (p_2/p_{02})^{(\kappa-1)/\kappa}}{1 - (p_2/p_{01})^{(\kappa-1)/\kappa}}$$

The loss coefficient ξ does not take the energy of the coolant flow into account. The thermodynamic energy loss ξ_{th} is just an extension of the loss definition above, but it includes the energy of the coolant flow (see Kost and Holmes 1985; Mee 1992):

$$\xi_{th} = 1 - \frac{(1 + c_m)\, W_2^2}{W_{2,is}^2 + c_m W_{a,is}^2}$$

$$= 1 - \frac{[1 - (p_2/p_{02})^{(\kappa-1)/\kappa}]\,(1 + c_m (T_{0a}/T_{01})}{1 - (p_2/p_{01})^{(\kappa-1)/\kappa} + c_m (T_{0a}/T_{01})\,[1 - (p_2/p_{0a})^{(\kappa-1)/\kappa}]}$$

In the following Table 3 the homogeneous flow values are listed.

The mixed out downstream flow angle and thermodynamic energy loss are plotted in Fig. 16 as a function of the real downstream Mach number. The losses have a maximum at Mach number 1. This behaviour is in analogy to the base pressure coefficient. Figure 15 presents the thermodynamic energy loss as a function of coolant flow rate. A distinct loss minimum at a moderate coolant flow rate is achieved, which is correlated with the base pressure coefficient. Therefore, it may

Table 3. Homogeneous flow values

Ma_{2is}	c_m [%]	p_2/p_{01}	p_{02}/p_{01}	Ma_2	w_2 [m/s]	ρ_2 [kg/m^3]	β_2 [°]	μ	ξ [%]	ξ_{th} [%]
1.01	0	0.524	0.938	0.95	301	0.733	29.2	1.06	9.1	9.1
1.05	2.5	0.496	0.944	1.01	315	0.706	30.0	1.07	7.5	6.3
1.22	0	0.403	0.935	1.07	355	0.607	29.5	1.05	6.5	6.5
1.22	0.8	0.404	0.940	1.17	356	0.609	29.0	1.03	6.1	5.2
1.23	1.4	0.399	0.938	1.18	358	0.603	28.9	1.02	6.1	5.0
1.21	2.5	0.409	0.931	1.15	352	0.613	29.8	1.03	7.1	6.2
1.34	0	0.342	0.951	1.30	387	0.542	32.3	1.11	4.0	4.0
1.35	0.8	0.338	0.958	1.32	390	0.540	32.3	1.11	3.4	2.6
1.36	1.4	0.332	0.949	1.32	391	0.531	32.6	1.09	4.1	3.0
1.35	2.5	0.335	0.940	1.31	389	0.533	31.7	1.05	4.8	4.2
1.45	0	0.300	0.949	1.40	407	0.494	34.9	1.12	3.7	3.7
1.45	0.8	0.294	0.950	1.41	410	0.487	34.8	1.12	3.6	2.8
1.45	1.4	0.293	0.943	1.41	410	0.485	34.7	1.12	4.0	3.0
1.45	2.5	0.293	0.932	1.40	408	0.483	34.6	1.08	4.8	4.2

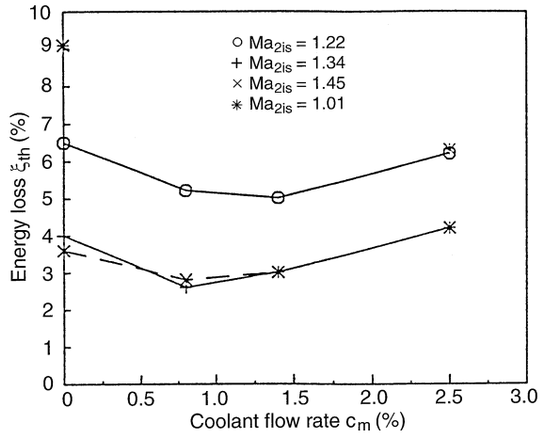

Fig. 15. Thermodynamic energy loss coefficient as a function of the coolant flow rate

be concluded that base pressure determines the losses at a thick turbine trailing edge and these losses may be influenced strongly by coolant ejection from the trailing edge. This statement will be proven in the following section.

7
An analysis of the separate contributions to loss

Schobeiri (1985, 1989), Köllen and Koschel (1985), Kost and Holmes (1985), or Mee (1992) have used the equations of conservation of mass, momentum and energy to analyse the mixing process downstream of the trailing edge in the presence of coolant ejection. Our analysis closely follows Kost and Holmes (1985):

The momentum equation in the axial direction for the case of trailing edge ejection will be given as an example:

$$\int_0^{t - d/\sin\alpha_b} (\rho_y v_y^2 \sin^2\alpha_y + p_y)\,\mathrm{d}y + p_b \frac{d - s}{\sin\alpha_b} + (\rho_c v_c^2 \sin^2\alpha_c + p_c)$$

$$\times \frac{s}{\sin\alpha_c} = (\rho_2 v_2^2 \sin^2\alpha_2 + p_2)\, t$$

where t is the pitch of the cascade and d the trailing edge thickness of the blade ($d/\sin\alpha_b$ is the projection of d into the cascade exit plane), s is the coolant slot width; furthermore the index y denotes the main flow at the cascade exit, b denotes the base region, c the coolant flow and 2 the mixed out downstream flow. The remaining equations of conservation of mass, momentum and energy may be written down in analogy to the above equation.

The above equation shows that the cascade exit plane was divided into three sections: the main flow including the profile boundary layers, the base region and the cooling slot. In the further procedure the main flow was considered as homogeneous, i.e. the losses produced by the boundary layer were included into the main flow loss at the cascade exit. In contrast to Schobeiri (1985) the base pressure p_b was taken from the experiment and as trailing edge thickness d an effective value was used because the exact separation locations were known from the experiment, (but the effective trailing edge thickness was only 0.4 mm smaller than the geometric one of 14 mm).

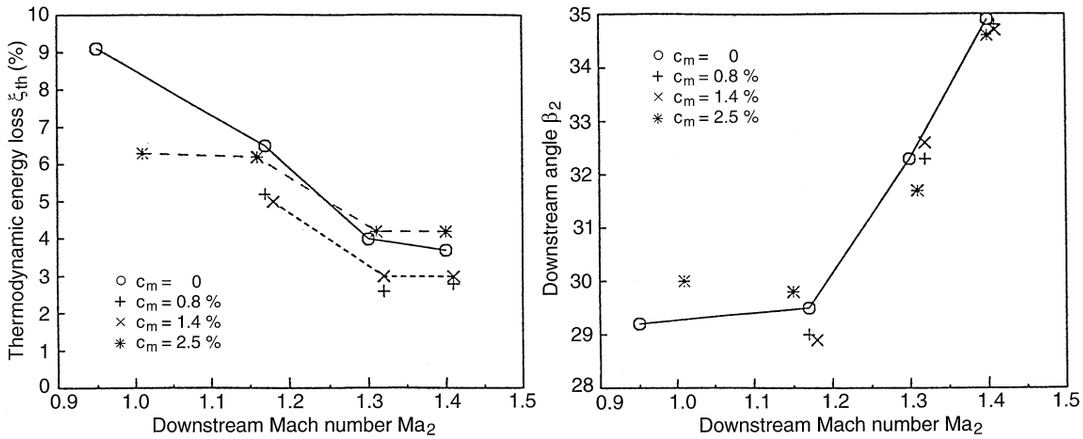

Fig. 16. Thermodynamic energy loss coefficient as a function of the downstream Mach number

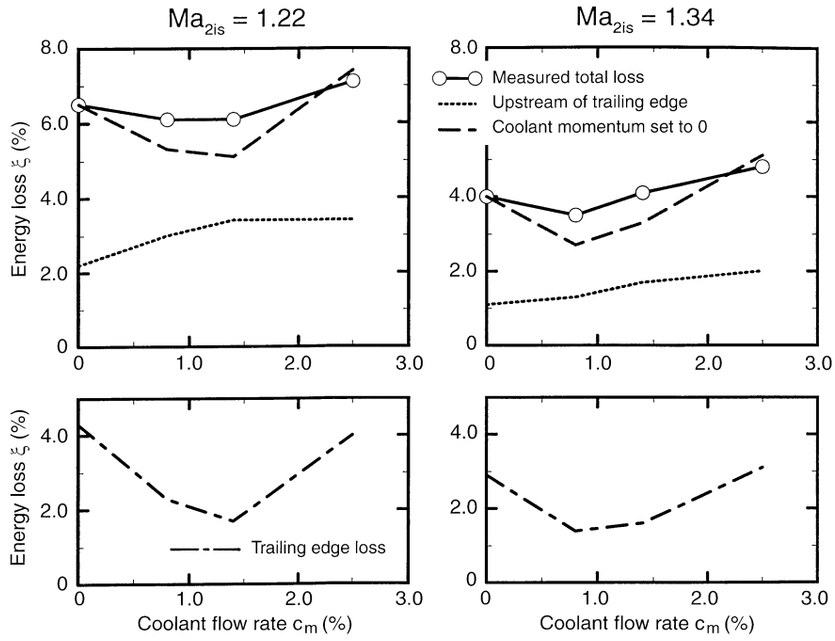

Fig. 17. The separate contributions to loss determined for two supersonic Mach numbers

As the mixed out flow values (station 2), the base pressure p_b and the coolant flow values (station c) had been measured, all values in the conservation equations were known with the exception of the main flow values at the cascade exit just upstream of the trailing edge (station y). The unknown values could be determined iteratively from the four conservation equations and from these values at station y the loss just upstream of the trailing edge can be derived. Figure 17 shows some results.

In Fig. 17 the loss coefficient ξ is shown as total loss curve as measured downstream, furthermore the separate contribution from the main flow upstream of the trailing edge (dotted curve) is shown and the main flow loss including the trailing edge loss (dashed curve). The dashed curve is produced by taking the evaluated main flow values from station y and the measured base pressure, setting the coolant momentum and slot width to zero and computing new downstream flow values by the conservation equations. The difference between dashed and dotted curve is just the contribution from the trailing edge which is plotted separately in the lower diagrams. It may be seen that trailing edge loss is a major contribution to total loss for the investigated flow case and the influence of coolant flow rate on this type of loss is tremendous. As explained in Chap. 4 the general effect of small coolant flow rates is to raise the base pressure and so decreasing trailing edge losses, but higher momentum coolant flow accelerates the base region fluid and so lowers base pressure and increases the trailing edge loss. Unfortunately the variation of base pressure with Mach number and coolant flow rate cannot be predicted reliably up to now, and especially the important influence of the

unstationary separation being beyond the scope of present-day Navier–Stokes codes.

A different effect is observed when investigating the contribution to loss which is caused by the mixing of the coolant flow with the mainstream flow. This has been extensively covered by Schobeiri and Pappu (1997). In Fig. 17 the difference between the dashed and the solid curve is the contribution to loss which is caused by the coolant momentum itself. An opposite development of this loss contribution with coolant flow rate is observed when compared to the development of trailing edge loss. For low coolant momentum the coolant mixing loss increases with coolant flow rate. This effect is due to the very low velocity (and total pressure) of the ejected coolant (see Table 1) which has to be accelerated to the downstream velocity v_2 by mixing with the mainstream flow. Near 2% coolant flow rate which corresponds roughly to a velocity ratio of 0.5 the loss due to coolant momentum is changing from a loss to a gain i.e. it lowers the total loss.

The loss or gain by mixing the coolant flow with the main stream depends of course not only on the coolant to mainstream momentum ratio but also on the angle of the coolant flow. If the ejection angle is roughly aligned to the main stream angle the dashed curve and the thermodynamic energy loss coefficient ξ_{th} give similar results as both take the coolant kinetic energy into account – the loss coefficient ξ_{th} by adding it in the denominator, the 'profile loss of the dashed curve' by subtracting it from the total loss. A parameter variation changing the angle and the temperature of the coolant has been reported by Kost and Holmes (1985) (see Fig. 4 in the cited paper).

The above analysis makes it clear that the coolant ejection from the trailing edge leads to two important effects which influence the resulting total loss: trailing edge loss, influenced via the base pressure and coolant flow mixing loss. It depends on the special configuration which of the two loss contributions is prevailing. Of course the two effects are linked together: base pressure is dependent on the ratio of coolant to main flow momentum, but in a manner not fully understood up to now. The type of unstationary flow downstream of the trailing edge which has been investigated by PIV and conventional methods in the present work, is undoubtedly connected with the type of separation at the trailing edge. The large scale vortical structures found by PIV have to be taken into account by the present-day numerical methods in order to make advances in the computation of such flows.

8 Conclusions

Schlieren images, pressure measurements by tappings and probes, and PIV recordings have been performed in order to investigate the aerodynamic effects of coolant ejection at the trailing edge of a transonic turbine blade model. The PIV measurement of flow velocity fields behind the trailing edge and the subsequent evaluation and analysis of pressure and velocity data yield detailed information on the features of such flow fields. In spite of difficult recording conditions the velocity data obtained is well suited for future comparison with data obtained by numerical simulations. Limits of imaging have been presented based on practical experiences and theoretical analysis. The following relations between the flow phenomena around the trailing edge and the coolant flow rate of cooling air in the case of trailing edge ejection could be demonstrated and quantitated by PIV and pressure measurements:

- A vortex street exists even in the case of supersonic cascade exit Mach numbers.
- This vortex street can be suppressed by trailing edge cooling air ejection at low coolant flow rates.
- The losses can be reduced by ejecting a small amount of coolant flow out of the trailing edge. For higher coolant flow rates the losses increase again. That indicates the existence of a optimum coolant flow rate with respect to the efficiency of the process.

Concerning the application of PIV in transonic turbine investigations it can be concluded that:

- The combination of flow field and pressure measurements enables the determination of the characteristic flow values such as Mach number, angle, and derived quantities such as thermodynamic energy loss ξ_{th}.
- Valuable flow field information can be obtained within a short measuring time, though imaging small tracer particles through density gradients is problematic and seeding of coolant flow has to be improved.

References

Adrian RJ; Yao C-S (1985) Pulsed laser technique application to liquid and gaseous flows and the scattering power of seed materials. Appl Opt 24: 44–52

Adrian RJ (1986a) Multi-point optical measurements of simultaneous vectors in unsteady flow – a review. Int J Heat Fluid Flow 7: 127–145

Adrian RJ (1986b) Image shifting technique to resolve directional ambiguity in double-pulsed velocimetry. Appl Opt 25: 3855–3858

Adrian RJ (1991) Particle-imaging techniques for experimental fluid mechanics. Ann Rev Fluid Mech 23: 261–304

Amecke J; Šafařik P (1995) Data reduction of wake flow measurements with injection of an other gas. DLR-Forschungsbericht 95-32, Köln

Cho Y-C (1989) Digital image velocimetry. Appl Opt 28: 740–748

Denton JD; Xu L (1989) The trailing edge loss of transonic turbine blades. ASME Technical Paper 89-GT-278

Goodman JW (1968) Introduction to fourier optics. McGraw-Hill Book Company, San Francisco

Hecht E; Zajac A (1974) Optics. Addison-Wesley, Reading, MA

Heinemann H-J; Lawaceck O; Bütefisch KA (1975) V. Karman vortices and their frequency determination in the wake of profiles in the sub- and transonic regimes. Symp. Transsonicum II, ed. K. Oswatitsch and D. Rues, Springer, Berlin, Heidelberg, New York

Höcker R; Kompenhans J (1991) Application of particle image velocimetry to transonic flows. Appl. of Laser Techniques to Fluid Mechanics, eds R.J. Adrian et al., Springer, Berlin, Heidelberg, Tokio, pp 415–434

Horlock JH (1966) Axial flow turbines. Robert E. Krieger Publishing Company, Malabar, USA

Humphreys WM; Bartram SM; Blackshire JL (1993) A survey of particle image velocimetry applications in langley aerospace facilities. AIAA Paper 93/041

Hunter WW; Nichols CE (eds.) (1985) Wind tunnel seeding systems for laser velocimeters. NASA Conf. Publication 2393, NASA Langley

Keane RD; Adrian RJ (1990) Optimization of particle image velocimeters. Part I: Double pulsed systems. Meas Sci Technol 1: 1202–1215

Keane RD; Adrian RJ (1992) Theory of cross-correlation analysis of PIV images. Appl Sci Res 49: 191–215

Köllen O; Koschel W (1985) Effect of film cooling on the aerodynamic performance of a turbine cascade. AGARD CP 390
Kompenhans J; Raffel M (1993) Application of PIV technique to transonic flows in a blow-down wind tunnel. Int. Symp. on Optical diagnostics in fluid and thermal flows, SPIE Proc. Vol 2005, pp. 425–436
Kost FH; Holmes AT (1985) Aerodynamic effect of coolant ejection in the rear part of transonic rotor blades. AGARD CP 390
Landreth CC; Adrian RJ; Yao CS (1988) Double pulsed particle image velocimeter with directional resolution for complex flows. Exp Fluids 6: 119–128
Mee DJ (1992) Techniques for aerodynamic loss measurement of transonic turbine cascades with trailing-edge region coolant ejection. ASME technical paper 92-GT-157
Meyers JF (1991) Generation of particles and seeding. Von Kármán Institute for Fluid Dynamics, Lecture Series 1991-05, Brussels
Melling A (1986) Seeding gas flows for laser anemometry conf on advanced instrumentation for aero engine components, AGARD-CP 399, paper 8
Molezzi MJ; Dutton JC (1993) Application of particle image velocimetry in high-speed separated flows. AIAA J. 31: 438–446
Motallebi F; Norbury JF (1981) The effect of base bleed on vortex shedding and base pressure in compressible flow. J Fluid Mech 110: 273–293
Oertel H (sen.); Oertel H (jun.) (1989) Optische Strömungsmeßtechnik. G. Braun Karlsruhe
Raffel M; Leitl B; Kompenhans J (1993) Data validation for particle image velocimetry. Appl. of Laser Techniques to Fluid Mechanics, ed R.J. Adrian et al., Springer, Berlin, Heidelberg, Tokio, pp 210–226
Raffel M; Kompenhans J (1994) Error analysis for PIV recording utilizing image shifting. 7. Int. Symp. on Appl. of Laser Techniques to Fluid Mech., Lisbon, Portugal, paper 35–5
Raffel M; Kompenhans J; Stasicki B; Bretthauer B; Meier GEA (1995) Velocity measurement of compressible air flows utilizing a high-speed video camera. Exp Fluids 17: 204–206
Raffel M; Kompenhans J (1995) Theoretical and experimental aspects of image shifting by means of a rotating mirror system for particle image velocimetry. Meas Sci Technol 6: 795–808
Raffel M; Höfer H; Kost F; Willert CE; Kompenhans J (1996) Experimental aspects of PIV measurements of transonic flow fields at a trailing edge model of a turbine blade. 8th Int Symp on Applications of Laser Techniques to Fluid Mechanics, Lisbon, Portugal, Paper 28-1
Rouland E; Vottier S; Lecordier B; Trinité M (1994) Cross-correlation PIV development for high speed flows with a standard CCD camera. 2nd Int. Seminar on Opt. Methods and Data Processing in Heat and Fluid Flow, pp. 9–20
Schäfer HJ (1995) private communication, ISL, St. Louis, France
Schobeiri MT (1985) Einfluß der Hinterkantenausblasung auf die hinter den gekühlten Schaufeln enstehenden Mischungsverluste. Forschung im Ingenieurwesen 51: 1
Schobeiri MT (1989) Optimum trailing edge ejection for cooled turbine blades. J Turbomach 111: 510–514
Schobeiri MT; Pappu K (1997) Zur Auslegung gekühlter Gasturbinenschaufeln mit optimaler Hinterkantenausblasung. Konstruktion 49: 33–39, Springer-VDI-Verlag
Sieverding CH; Decuyper M; Colpin J; Amana O (1976) Model tests for the detailed investigation of the trailing edge flow. Convergent Transonic Turbine Cascades, ASME Technical Paper 76-GT-30
Sieverding CH; Stanislas M; Snoeck J (1980) The base pressure problem in transonic turbine cascades. J Eng Power 102: 711–718
Sieverding CH (1982) The influence of trailing edge ejection on base pressure in transonic turbine cascades. ASME Technical Paper 82-GT-50
Sinha SK (1988) Improving the accuracy and resolution of particle image or laser speckle velocimetry. Exp Fluids 6: 67–68
Solf KD (1975) Fotografie: Grundlagen, Technik, Praxis. Fischer-Verlag
Towers CE; Bryanston-Cross PJ; Judge TR (1991) Application of particle image velocimetry to large-scale transonic wind tunnels. Optics & Laser Technol 23: 289–295
Willert CE; Gharib M (1991) Digital particle image velocimetry. Exp Fluids 10: 181–193
Willert CE (1996) The fully digital evaluation of photographic PIV recordings. Appl Sci Res 56: 79–102